Cavity flows of elastic liquids: Purely elastic instabilities

Peyman Pakdel and Gareth H. McKinley
Division of Engineering and Applied Sciences, Harvard University, Cambridge, Massachusetts 02138

(Received 3 September 1997; accepted 16 January 1998)

Experimental observations of a purely elastic flow instability occurring in the lid-driven cavity flow of two semi-dilute polymer solutions are reported and the effect of cavity aspect ratio on the dynamical structure of the unstable flow is quantitatively investigated. The spatial and temporal characteristics of the secondary flow are measured using flow visualization, laser Doppler velocimetry, and digital particle image velocimetry. At the onset conditions the disturbances appear in the form of spatially periodic flow cells which propagate along the neutral direction of the cavity. The secondary flow structure is analogous to the Taylor–Görtler vortices observed in inertially driven hydrodynamic instabilities. The critical onset conditions for two elastic test fluids and five different aspect ratios correlate with a recently proposed dimensionless stability criterion which incorporates measures of the local streamline radius of curvature and the non-Newtonian normal stresses in the flow domain. © *1998 American Institute of Physics.* [S1070-6631(98)00505-4]

I. INTRODUCTION

The lid-driven cavity flow is the motion of a fluid in a rectangular box generated by a constant translational velocity of one side while the other sides remain at rest. In the two-dimensional limit, the flow consists of a planar recirculatory fluid motion confined by rectangular boundaries. The lid-driven cavity flow of Newtonian liquids has been the subject of extensive computational and experimental studies over the past 30 years. These studies have been motivated by the geometrical simplicity of the flow domain, the existence of stress singularities at two corners, and the complex dynamical structure that arises from the onset of inertial instabilities.[1]

The lid-driven cavity flow poses a complex fluid mechanics problem in which regions of strong shear near the top moving plate, vortical motion in the central core, and corner flows simultaneously exist and interact in a system with closed streamlines. Inertial effects play a dominant role in governing the kinematical structure of the fluid motion and stability of cavity flows of Newtonian liquids. Inertial effects are quantified by the Reynolds number, defined as

$$\mathrm{Re}=\frac{LU\rho}{\mu}, \tag{1.1}$$

where L is the width of the cavity, U is the magnitude of the imposed top-plate velocity, and μ and ρ are the constant viscosity and density of the liquid, respectively. At negligibly small Reynolds numbers, the Newtonian cavity flow is fore-aft symmetric. Increasing the Reynolds number breaks this symmetry and eventually at a critical Reynolds number, $\mathrm{Re}_{\mathrm{crit}}\approx 500$, the flow becomes three dimensional via the amplification of spatial and temporal disturbances.[2] The driving mechanism of these inertial instabilities is similar to that leading to the growth of classical Taylor vortices in the Couette device[3] and to the related inertial instabilities that result in the formation of Görtler vortices in boundary layer flows along curved surfaces.[4]

This hydrodynamic instability is driven via the nonlinear coupling term, $\mathbf{v}\cdot\nabla\mathbf{v}$, in the equation of motion[1] and is characterized by the emergence of Taylor–Görtler-like (TGL) vortices that are spatially periodic in the neutral direction of the flow and contain streamwise vorticity. Recent numerical linear stability analyses and experimental flow visualizations provide a consistent quantitative understanding of the dynamical structure of the inertial instabilities in recirculating cavity flows of Newtonian liquids. Flow visualization experiments indicate that the secondary motions are initially time independent ($\mathrm{Re}_{\mathrm{crit}}\approx 500$) and characterized by a steady spatially periodic structure in the spanwise direction. Increasing the Reynolds number beyond a value of $\mathrm{Re}\approx 825$ results in a further flow transition that leads to evolution of a time-dependent traveling-wave mode.[5]

Cavity flows become intrinsically more complex when the fluid rheology is non-Newtonian. These complications arise as a result of the polymeric contribution to the deviatoric stress field, which is strongly coupled to the fluid kinematics and is a function of an integral history of local rates of deformation experienced by a fluid element moving along a closed streamline. The presence of a viscoelastic fluid memory, shear thinning effects in the material functions, nonzero normal stress differences, and the complex extensional rheological behavior of non-Newtonian fluids can each alter the fluid kinematics in the cavity geometry.

Leong and Ottino appear to have been the first to experimentally examine the effect of viscoelasticity in cavity flows.[6] They conducted a comparative experimental flow visualization study of time-periodic flows in a viscous Newtonian fluid and in an ideal elastic Boger fluid.[7] These ideal elastic fluids are synthesized by dissolving a small amount of a high molecular weight polymer in a viscous Newtonian solvent. In addition to exhibiting an almost constant shear viscosity over a wide range of shear rates, they display appreciable fluid viscoelasticity and large first normal stress differences in steady shear flows. In their flow visualization experiments with a passive dye tracer, Leong and Ottino ob-

served that the extent of mixing was weaker in the non-Newtonian case than in the corresponding Newtonian flow under similar time-periodic boundary conditions. Analogous viscoelastic effects have also been observed in time-periodic mixing flows generated in the eccentric cylinder geometry.[8,9]

Cavity flows of Generalized Newtonian fluids have been the subject of two computational studies; Reddy and Reddy[10] investigated the heat transfer effects in steady three-dimensional cavity flows of power-law and Carreau fluids, and Isaksson and Righdal[11] examined the steady streamline patterns and local pressure distribution via two-dimensional numerical simulation of a power-law fluid.

In order to investigate the first effects of fluid elasticity, numerical computations of lid-driven cavity flow were performed by Mendelson *et al.*[12] using the second order fluid model. It is well known that the Newtonian velocity field satisfying the Stokes equations is a unique solution to the equations of motion for steady planar creeping flows of a second order fluid.[13] Based on these uniqueness and existence theorems, Mendelson *et al.*[12] show that finite element simulations with the second order fluid model cannot accurately resolve the steep gradients in viscoelastic stress that develop near the upper corners of the sliding plate. Furthermore, as pointed out by these authors, such numerical simulations cannot provide information on the temporal stability of the flow and in fact, linear stability analysis has shown that the steady planar flow of the second order fluid model is temporally unstable at all finite Deborah numbers.[14]

Pakdel, Spiegelberg, and McKinley[15] have conducted kinematic measurements of the steady two-dimensional motion of Boger fluids in the cavity geometry at negligible Reynolds numbers using laser Doppler velocimetry (LDV) and digital particle image velocimetry (DPIV). They observe that viscoelasticity breaks the fore-aft symmetry of the flow structure observed in the Stokes flow regime. The geometric center of the core vortex region shifts slightly in the upstream direction (i.e., in the opposite direction to the translational velocity of the lid) and the magnitude of this shift increases as the imposed velocity of the driving boundary wall is increased. The magnitude of the velocity gradients are enhanced in the corner regions near the moving plate. The local maxima in the velocity gradients are spatially located slightly away from the corners ($\approx 0.2L$) and appear in regions where the fluid streamlines exhibit significant curvature.

To quantify the non-Newtonian effects in cavity flows, Pakdel *et al.*[15] define two-dimensionless groups; the Deborah and the Weissenberg numbers. The Deborah number is defined as

$$\mathrm{De} = \lambda U/L, \tag{1.2}$$

and the Weissenberg number is defined as

$$\mathrm{Wi} = \lambda U/H, \tag{1.3}$$

where U is the constant translational speed of the upper lid, λ is a characteristic relaxation time of the fluid, L is the width, and H is the height of the cavity. With these definitions, De quantifies a ratio of the fluid viscoelastic memory to a characteristic residence time in the system, $t_{\mathrm{flow}} = L/U$, and Wi provides a dimensionless measure of the magnitude of the imposed shear rate, $\dot{\gamma} = U/H$. The non-Newtonian normal stress differences in the fluid are strong nonlinear functions of the shear rate and consequently scale with Wi.

Along with these groups a purely geometrical parameter, namely the aspect ratio Λ, can be defined as

$$\Lambda = H/L. \tag{1.4}$$

This parameter quantifies the relative importance of the two characteristic length scales in the cavity geometry. In the case of deep narrow slots ($H \gg L, \Lambda \gg 1$), the width of the cavity governs the kinematics of the main circulation region, and in case of the long shallow channels ($H \ll L, \Lambda \ll 1$) the height of the cavity plays the determining role in establishing the streamline patterns of the recirculating shear flow in the bulk of the cavity. The collective set of dimensionless groups De, Wi, and Λ, together with a knowledge of the fluid material functions, spans a parameter space that fully specifies the operating condition of cavity flows of viscoelastic fluids at negligible Reynolds numbers.

Over the past eight years, viscoelastic instabilities occurring at negligibly small Reynolds numbers have been the subject of intense theoretical and experimental studies. These instabilities, commonly referred to as *purely elastic instabilities*, are entirely absent in the corresponding flows of Newtonian fluids and are driven by mechanisms associated with elastic normal stress differences rather than inertial nonlinearities in the equation of motion. The nonlinear coupling among the components of the Cauchy momentum equations is embedded in the nonlinear constitutive relationships that describe the evolution of the viscoelastic stress, τ, in flowing polymeric processes. This nonlinear coupling gives rise to terms of the form $\mathbf{v}\cdot\nabla\boldsymbol{\tau}$ and $\nabla\mathbf{v}\cdot\boldsymbol{\tau}$ which scale independently of the Reynolds number in the governing equation set.

Earlier studies on the subject of elastic instabilities date back to Giesekus[16] who reported onset of elastic instabilities in Taylor–Couette flow of a shear-thinning fluid at a Reynolds number of 10^{-2}. With the synthesis of ideal elastic Boger fluids,[7] it became possible to isolate the effect of elasticity in the absence of additional complicating phenomena such as shear thinning in the fluid viscosity and the associated increase in inertial effects. Purely elastic instabilities in constant viscosity fluids were first reported by Muller, Larson, and Shaqfeh[17] who observed clear indications of a flow instability while attempting to perform rheological measurements of Boger fluids in a Taylor–Couette device. Their study initiated a number of computational and experimental studies in the Taylor–Couette geometry over the past eight years (see, for example, Refs. 18–20).

Similar studies of torsional flow in the cone-and-plate geometry,[21–24] and the coaxial parallel plate geometry,[25,26] the axisymmetric contraction flow,[27] and in the wake behind a cylinder[28] indicate that elastic instabilities are not specific to a flow geometry but occur in many complex flow fields. The critical onset conditions are sensitive functions of the fluid rheology and of the characteristic geometric parameters governing the flow configuration. Furthermore, these numerical and experimental studies have all documented a similar geometrical pattern in this class of instabilities,

namely the development of a spatially periodic cellular structure in the neutral direction which may, or may not, be time dependent. The review articles of Larson[29] and Shaqfeh[30] provide a detailed picture of the recent research on elastic instabilities, and identify specific mechanisms for the nonlinear coupling between the momentum and constitutive equations.

In a recent study closely related to the cavity flow geometry, Grillet and Shaqfeh[31] observed elastic instabilities in their modified Taylor–Couette experiments with Boger fluids. In this work a meridional block was inserted in the cylindrical Taylor–Couette device which created a local recirculating pressure-driven Taylor–Dean motion upon steady rotation of either the inner or the outer cylindrical wall. In this configuration, elastic instabilities were observed near the block at critical speeds which were markedly lower than the critical values observed far from the block in the unmodified Taylor–Couette flow. This indicates that the local recirculation near the inserted block is responsible for initiating instabilities at lower critical speeds. In the limit of narrow gaps between the inner and outer cylinders, the azimuthal curvature can be neglected and this geometry can be unraveled and viewed as a cavity flow with a very small aspect ratio, $\Lambda \to 0$.

In a companion study to the present work, Pakdel and McKinley[32] conducted a series of flow visualization experiments of cavity flows of Boger fluids in a more moderate range of aspect ratios $0.25 \leqslant \Lambda \leqslant 4.0$ and reported observations of elastic instabilities for all aspect ratios. Based on these observations and consideration of previous studies of elastic instabilities occurring in various geometries, they proposed a general dimensionless stability criterion that can be used to quantify the onset of elastic instabilities based on the local kinematics of the flow and the elastic properties of the fluid. This criterion was further developed in a more detailed study,[33] to incorporate the effects of shear thinning in the material functions, changes in the solvent viscosity, and a spectrum of relaxation times. Comparisons with existing data in the literature showed that the proposed stability criterion is successful in providing a sufficient condition that can characterize the onset of elastic instabilities for isothermal fluid motions within many geometries with curvilinear streamlines. This is consistent with theoretical studies which indicate that there should exist universal destabilizing mechanisms that depend on the local fluid kinematics and stress distributions, which are themselves functions of the fluid rheology and global dimensionless geometrical parameters characterizing the flow.

In this study, we expand the results of Pakdel and McKinley[32] and Pakdel *et al.*[15] and provide detailed experimental results on the spatial and temporal dynamical structure of the purely elastic instabilities that develop in cavity flows over a range of aspect ratios ($0.25 \leqslant \Lambda \leqslant 4.0$). We use LDV and DPIV to probe the kinematics of the secondary motions in the cavity flows of two ideal elastic Boger fluids. In the next section we describe our experimental apparatus and operating conditions, and characterize the rheology of the viscoelastic fluids used in our experiments. We then report our experimental results including global flow visualization of the instabilities, plus quantitative measurements of the spatial and temporal frequency of the unstable modes and conclude with an analysis of the recently proposed dimensionless criterion for elastic instabilities and its application in viscoelastic cavity flows.

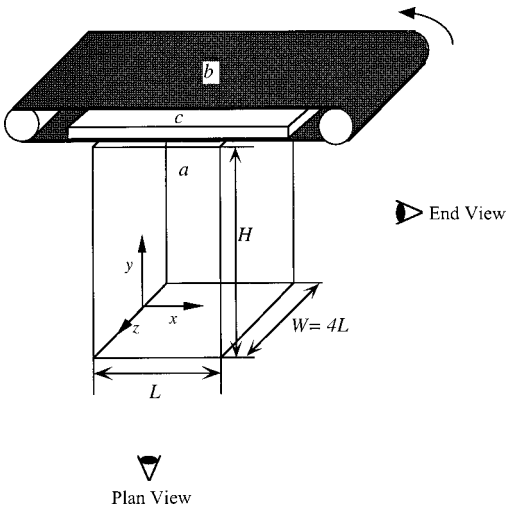

FIG. 1. Schematic diagram of the experimental apparatus: (a) cavity cell; (b) translating belt; (c) pressure plate.

II. EXPERIMENTAL CONDITIONS

A. Geometry

A schematic diagram of the apparatus is shown in Fig. 1. The geometric specifications of the test cell have been described previously,[15] and here we briefly describe the pertinent information related to the present experimental study. The cavity cell is constructed with $\frac{1}{2}$-in. Plexiglas and the cavity dimensions are $L = 2.54$ cm, $W = 10.16$ cm, where W is the length in the neutral direction. The depth of the cavity, H, can be varied in the range $1/4L \leqslant H \leqslant 4L$, by using Plexiglass inserts to provide aspect ratios in the range of $0.25 \leqslant \Lambda \leqslant 4$, respectively. The aspect ratio in the spanwise direction is $W/L = 4$ and can be altered to $W/L = 8$ by using suitable inserts. The fluid motion is generated by translating a smooth continuous polyester belt over the top of the cavity. The maximum linear belt speed is approximately $U \approx 5.0$ cm/s or $2L$/s.

The cavity cell provides visual access from all three principal planes in the Cartesian coordinate system shown in Fig. 1. The x-y plane at the midpoint of the channel width is the cross section of the flow in which our previous two-dimensional cavity flow measurements were performed. Following the onset of hydrodynamic instabilities, the orthogonal views of the x-z and y-z planes provide additional information about the kinematic structure of the disturbances in the neutral z-direction. The test fluids are seeded with minute amounts of small Mica flakes which reflect the incident light with varying intensity depending on the direction and uniformity of the local velocity field. In the steady base flow regime, these particles reflect a uniform background light intensity in the x-z and y-z planes. However, following

TABLE I. Viscometric properties of the two PIB Boger fluids.

Rheological parameter	Fluid A-0.20 wt. % PIB	Fluid B-0.35 wt. % PIB
$\Psi_{1,\ \text{plateau}}$ [Pa s^2]	16	60
η_0 [Pa s]	24	35
η_s [Pa s]	19	23
λ_s [s]	1.6	2.5
λ_r [s]	8.5	15
β	0.79	0.66

the onset of an hydrodynamic instability, they develop nonuniform effective light patterns in the neutral direction depending on the relative fluid velocity and particle orientation with respect to the incident light. A similar visualization technique has been used by Baumert and Muller[34] to document the complex spatio-temporal dynamics following the onset of purely elastic instabilities in Taylor–Couette flow.

In addition to visualization of the global dynamics, quantitative kinematic measurements are performed using laser Doppler velocimetry and digital particle image velocimetry, details of which are given elsewhere.[15,35] The onset of instabilities are detected both by visual inspection and by LDV measurements. Spatial wave numbers are determined from photographs and verified by rapidly scanning the cell with the laser probe using a translating stage while simultaneously collecting LDV data. The temporal frequencies are obtained from time-series analysis of velocity measurements made using the LDV system at a fixed point in space. Each experimental run is carried out with a fresh batch of each test fluid in order to reduce possible effects of polymer degradation.

B. Fluid rheology

A viscous polybutene (PB) oil (Amoco Indopol H300) with a mass-averaged molecular weight of approximately 1000 g/mole is used as the Newtonian base fluid. The elastic Boger fluids are prepared by dissolving 0.20 wt. % and 0.35 wt. % of high molecular weight polyisobutylene (PIB) (Exxon L-120, $M_w \sim 1.2\times 10^6$ g/mole) respectively in the PB oil.

The rheological properties of these fluids show similar characteristics to those reported previously in the literature.[36,15] The viscometric properties of both solutions are summarized in Table I.

As the rheological characterization of Quinzani *et al.*[36] demonstrates, the first normal stress coefficient of semidilute Boger fluids generally show two plateaulike regions; a zero-shear-rate plateau at very small deformation rates, and a second region at an intermediate shear rate range of $0.1 \leqslant \dot{\gamma} \leqslant 10\ \text{s}^{-1}$. At higher shear rates of $\dot{\gamma} > 10\ \text{s}^{-1}$, the first normal stress coefficient monotonically shear thins. For these fluids the zero-shear-rate limit Ψ_{10} is difficult to measure directly with reasonable accuracy since the normal force becomes indetectably small, although its magnitude can be inferred from linear viscoelastic measurements of the quantity $2\eta''/\omega$ at low frequencies.[36] However, in Table I, we choose to report the average values of Ψ_1 measured experimentally in the second plateau region since this range is consistent with the operating range of shear rates in our cavity flow geometry.

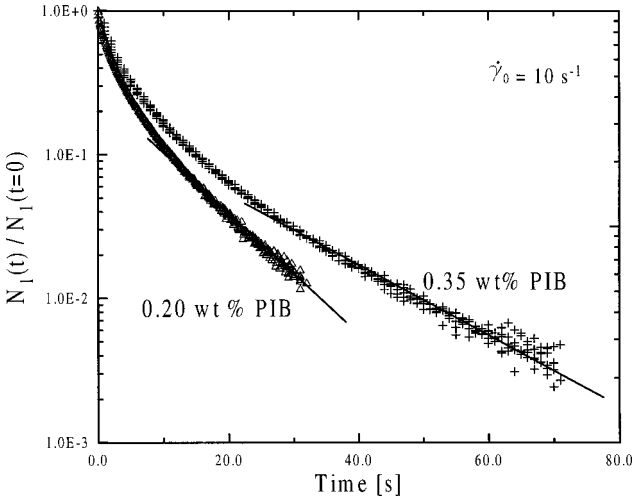

FIG. 2. Relaxation of the first normal stress difference $N_1^-(t)$ with time following cessation of steady shear flow for the 0.20 and 0.35 wt. % PIB solutions. The initial steady shear flow was at a shear rate of $\dot{\gamma}_0 = 10\ \text{s}^{-1}$.

The shear viscosity of both fluids remains relatively constant over a wide range of shear rates $\dot{\gamma} \leqslant 100\ \text{s}^{-1}$ beyond which it slowly shear thins. The values of the dimensionless parameter $\beta = \eta_s/\eta_0$, characterizing the relative contribution of the Newtonian solvent to the total viscosity in viscoelastic constitutive equations such as the Oldroyd-B model, are in the range of $0.6 \leqslant \beta \leqslant 0.8$.

The time constant λ_s computed from the viscometric data measured in steady simple shear flow is defined as

$$\lambda_s = \frac{\Psi_{1,\text{plateau}}}{2(\eta_0 - \eta_s)},$$

where η_s is the solvent viscosity. As it has been noted elsewhere,[30] different rheological tests provide differently weighted moments of the relaxation spectrum present in any macromolecular material. For completeness we also report another characteristic time constant λ_r in Table I obtained from measurements of the normal force relaxation following the cessation of steady shear flow as shown in Fig. 2. Matching the entire nonlinear relaxation observed in the decaying first normal stress difference $N_1^-(t)$ requires consideration of a multimodal constitutive model; however, the data beyond the first few seconds can be accurately represented via a single relaxation time, λ_r. The ratio of relaxation times, λ_r^A/λ_r^B for the two fluids A and B, appears to scale well with the corresponding ratio of λ_s^A/λ_s^B. Relevant values of the dimensionless numbers characterizing viscoelastic effects in the cavity flow can be based on either of these characteristic time scales and for clarity are denoted De_s or De_r as appropriate.

In the context of elastic instabilities, it is appropriate to ask which relaxation time (or Deborah number) is appropriate for correlating experimental results. This issue has been briefly discussed in Ref. 30 and has been considered in detail by Larson *et al.*[37] In the latter work, experimental measure-

ments of the steady and transient shear rheology were fitted with a K-BKZ integral constitutive model with a continuous spectrum of relaxation times characterized by a power-law exponent, p. For this model the ratio of average to the longest relaxation time (denoted by $\bar{\lambda}/\lambda_1$ in Ref. 37) is given by $\lambda_s/\lambda_r=(1-p)$. For solutions of 0.1 wt. % PIB in PB and polystyrene in oligomeric styrene, Larson *et al.* report that the values of $p\approx 0.75$ and $p\approx 0.82$, respectively, provide the best correlations to the rheological data. For the fluid properties given in Table I, we find $p_A\approx 0.81$ and $p_B\approx 0.83$, in good agreement with the previous study. Larson *et al.*[37] also compared theoretical predictions of elastic instabilities in the Taylor–Couette flow (using the K-BKZ model) with experimental stability observations and suggested that a Deborah number based on the geometric mean of the average and longest relaxation times may provide the best measure of the elasticity in the flow. In the present work we report our stability observations in terms of both De_r and De_s, and a geometric mean can easily be computed from these values if desired.

III. RESULTS

A. Global flow visualization

To detect the evolution in the secondary flow structure following onset of an elastic instability, the flow cell is illuminated with a diffuse background white light source. In the absence of any flow structure in the neutral direction, the Mica flakes reflect the incident light uniformly. When the flow becomes nonuniform, bands of darker and brighter light intensities develop in the neutral z-direction.

The belt speed is increased in small discrete steps while ample observation time (5–10 min) between increments is given for the possible development of elastic instabilities. When a discernable flow structure appears in the neutral direction, the critical linear belt speed U_{crit} is recorded. In Fig. 3 an *end view* of the y-z plane of the cavity cell is shown along the x-axis and the spatial scale of the cell is shown via a ruler with centimeter gradations. The direction of motion of the belt is normal to the viewing plane and outward from the page. In the stable region, the reflected light intensity appears uniform [Fig. 3(a)]. However, at the critical onset condition, $\mathrm{De}_{s,\mathrm{crit}}\approx 0.35$, a new spatial structure develops in the flow as shown in Fig. 3(b). The aspect ratio of the cavity in Fig. 3 is $\Lambda=1$, and the aspect ratio in the neutral direction is $W/L=4$. The bright regions in Fig. 3(b) divide the flow domain into three cellular regions.

In Fig. 4, the flow structure at the onset conditions is shown for a cavity with an identical aspect ratio of $\Lambda=1$ but with a neutral direction aspect ratio of $W/L=8$. The critical Deborah number is found to be the same for both cases and the number of cellular regions in the $W/L=8$ case is doubled to six. This observation indicates that the elastic instabilities are driven primarily from consideration of the stable two-dimensional planar base flow in the x-y plane and the three-dimensional flow regions near the end walls do not drive the flow into the three-dimensional regime, at least for cavities of size $W/L\geqslant 4$.

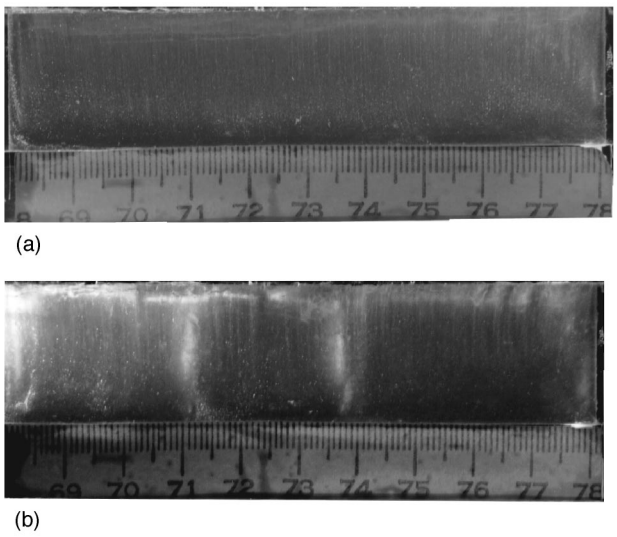

FIG. 3. Flow visualization of elastic instability in a square cavity ($\Lambda=1$; plan view). The end view of the cavity flow is presented in which the imposed velocity is normal to the plane of view and outward from the paper. (a) The stable flow at $\mathrm{De}_s=\mathrm{Wi}_s=0.25$; (b) the unstable flow following the onset of elastic instability at critical flow conditions of $\mathrm{De}_s=\mathrm{Wi}_s=0.35$.

As we show below, these cellular structures are in fact traveling waves which propagate along the neutral (z) direction of the cavity. The LDV time series presented in Sec. III B show that in a time-averaged sense the flow structure is periodic at small supercritical Deborah numbers. However, at any instant of time, analysis of the video recording shows that cells are continuously created and destroyed near either end wall, and this accounts for the uneven spanwise distribution observed in Figs. 3(b) and 4. In analogous Taylor–Couette studies, the neutral direction aspect ratio, W/L, is typically very large due to the small gap width in the flow cell. However, in cavity geometries appearing in industrial applications, this aspect ratio is much smaller and nonsymmetric structures arising from the influence of end effects and geometric imperfections are more likely to be observed.

In Fig. 5 we show similar end views (in the y-z plane) of the cellular structures following onset of elastic instability for deeper cavities with aspect ratios of $\Lambda=2$ and $\Lambda=3$. The critical Deborah numbers are approximately the same as those recorded for the square cavity $\Lambda=1$. Furthermore, the number of primary cells remains unchanged at three, as observed for the case of $\Lambda=1$. The separation between the primary recirculating vortex structure near the translating plate and the weaker secondary vortex near the stationary

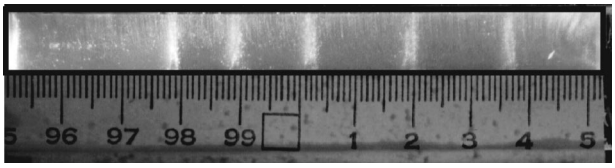

FIG. 4. Flow visualization of the elastic instability in a square cavity ($\Lambda=1$, end view). The aspect ratio in the neutral direction is $W/L=8$. The imposed velocity is normal to the plane of view in the outward direction ($\mathrm{De}_s=\mathrm{Wi}_s=0.35$).

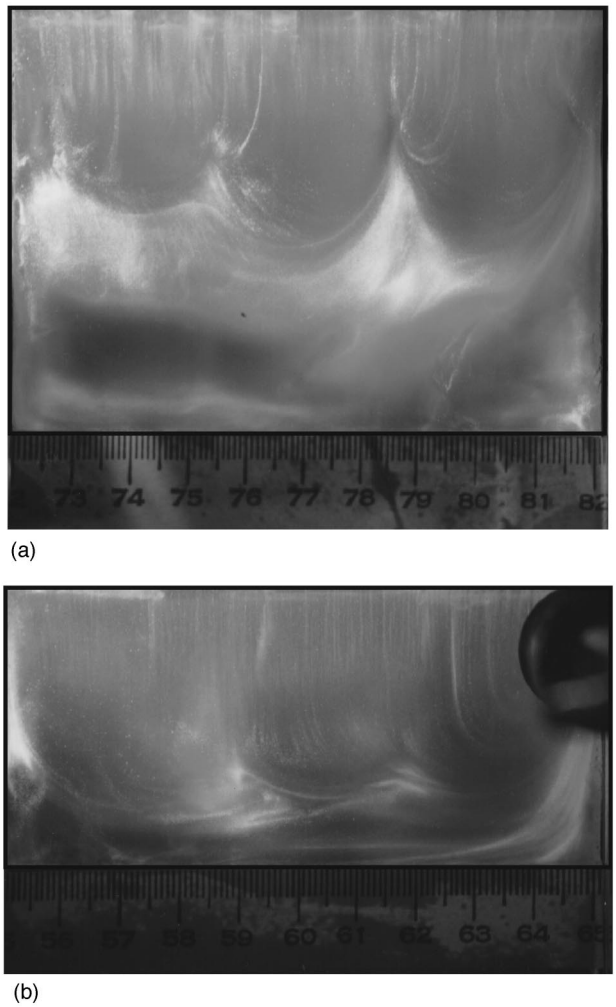

FIG. 5. Flow visualization of elastic instabilities in cavity flows (end view) with (a) $\Lambda=3$, $\mathrm{De}_s=0.37$, $\mathrm{Wi}_s=0.12$, (b) $\Lambda=2$, $\mathrm{De}_s=0.35$, $\mathrm{Wi}_s=0.18$. The imposed velocity is normal to the plane of view and oriented outward from paper.

base of these deep cavities can be clearly discerned. The uniformity of the reflected light in these lower regions indicates that, at least within the time scale of an experimental run (≈ 1 h), there is little dynamical evolution in this weak recirculation region for either aspect ratio.

Decreasing the aspect ratio of the cavity, however, has a different effect. In Fig. 6, the cellular structures observed at the critical onset conditions are shown in a *plan view* (i.e., in the x-z plane) for shallow cavities with aspect ratios of $\Lambda=0.5$ and $\Lambda=0.25$. The critical values of the Deborah number and Weissenberg number are significantly different from those recorded for the square cavity ($\Lambda=1$). The critical Deborah number decreases as the aspect ratio decreases, indicating that the instabilities are initiated at smaller belt speeds than for the square cavity. On the other hand, the critical Weissenberg number increases with decreasing aspect ratios, indicating the increasing magnitude of the shear rate near the moving belt and the resulting enhancement of elastic normal stress differences in the cell. The relation between these two dimensionless groups at the critical onset conditions is a delicate balance between these two length

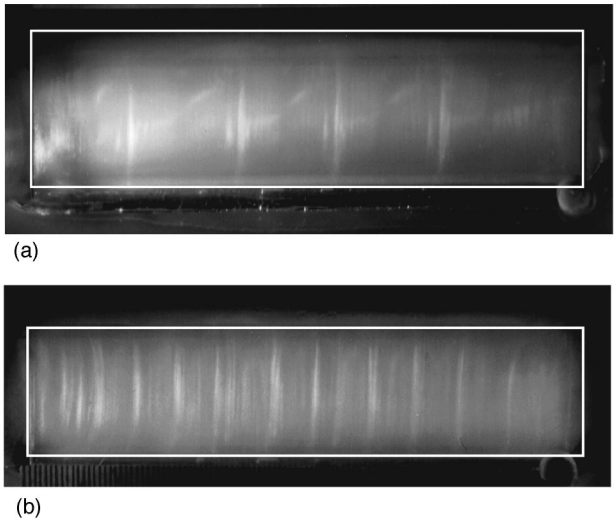

FIG. 6. Flow visualization of elastic instabilities in cavity flows (plan view) with (a) $\Lambda=0.5$, $\mathrm{De}_s=0.29$, $\mathrm{Wi}_s=0.58$, (b) $\Lambda=0.25$, $\mathrm{De}_s=0.25$, $\mathrm{Wi}_s=1.0$. The imposed velocity is parallel to the plane of view and oriented in the upward direction.

scales in the system, namely, L and H, which in turn give rise to two time scales in the cavity geometry.

Increasing the belt speed to values significantly greater than U_{crit} excites higher order wave number disturbances. In this region the cavity operates in a time-dependent mixing flow regime with the cellular structures rapidly fluctuating in extent and configuration. This transition to the mixing flow regime can be better characterized by the spatio-temporal frequency measurements presented in the next section.

B. Local frequency measurements

To probe the dynamical structure of the instabilities observed via flow visualization, temporal and spatial frequencies are measured as the imposed lid velocity is increased. In Fig. 7, time-series measurements of the y-component of the velocity are shown as a function of increasing Deborah number. These measurements are performed close to the geometrical center of the primary recirculation in the cavity at $x/L=0.5$, $y/H=0.8$, $z/W=0.0$ for an aspect ratio of $\Lambda=1$.

In the stable region, $\mathrm{De}_s=0.2$, the vertical component of the velocity at this position remains almost zero as a function of time. At the critical onset condition, $\mathrm{De}_{s,\mathrm{crit}}\approx 0.35$, the instability initially develops as a slowly traveling sinusoidal wave in the cavity with a period of approximately 600 s. Increasing the Deborah number beyond the critical limit to $\mathrm{De}_s=0.72$ decreases the period of the traveling wave to values on the order of 100 s. At higher Deborah numbers, the primary mode is combined with higher frequency disturbances which ultimately result in rapid aperiodic fluctuations of the local velocity field in the cavity.

In Fig. 8, the power spectral density (PSD) is shown for a set of time-series measurements obtained at the same location in the cavity. At weakly supercritical Deborah numbers ($\mathrm{De}_s/\mathrm{De}_{s,\mathrm{crit}}\approx 1.3$), the instability is characterized by a single mode with a frequency $f_1=7.9\times 10^{-3}$ Hz. Increasing

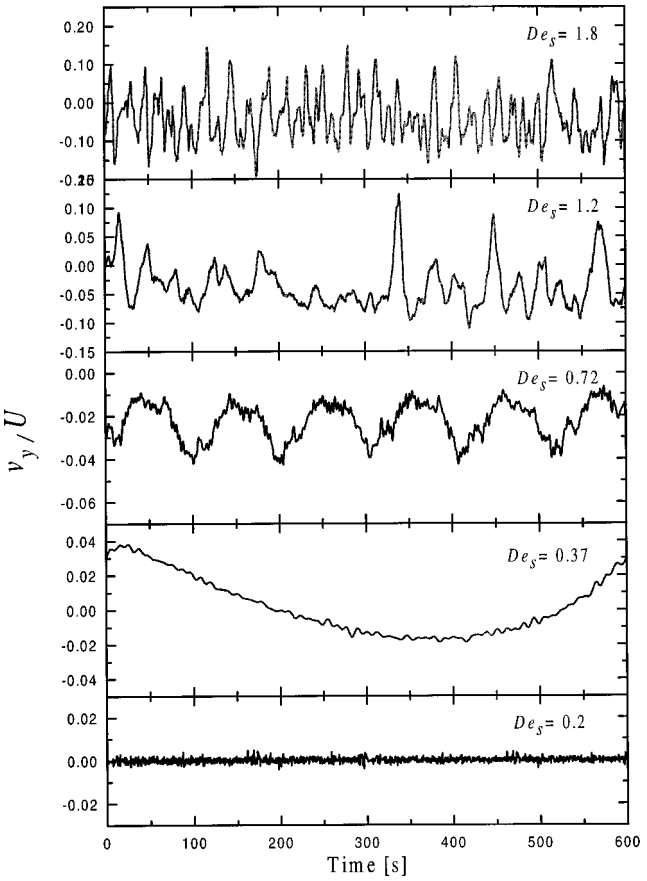

FIG. 7. Time-series measurements of the vertical y-component of the velocity field at $x/L=0.5$, $y/H=0.8$, $z=0.0$ in a square cavity ($\Lambda=1$); the evolution of the elastic instability as a function of the imposed lid velocity.

the Deborah number further, excites the second harmonic and other higher frequency modes ultimately creating a mixing-type flow regime.

In Fig. 9, the primary temporal frequency, f_1, is plotted against the Deborah number for the three dynamically distinct aspect ratios of $\Lambda=1,0.5,0.25$. The spectral resolution of the slowly varying time-periodic flow that develops beyond a critical Deborah number is governed by the total duration of the velocity time series, T. For most of the data presented here, the time-series span a period of $T \approx 200-300$ s leading to a spectral resolution of approximately $\pm 1/T \approx 0.003$ Hz indicated by the error bar on the first data point in Fig. 9.

The temporal frequencies measured in deeper cavities with aspect ratios greater than one are similar to the $\Lambda=1$ case. As is shown in Fig. 9(a), the magnitude of the primary frequency initially increases with Deborah number and gradually approaches a plateau value as the flow evolves into the mixing regime. The frequencies are higher in the $\Lambda=0.25$ cavity than in the larger aspect ratios. In Fig. 9(b) the same frequencies are scaled with the characteristic residence time of the system L/U and are plotted against the Deborah number. The primary dimensionless frequency appears to decline dramatically for $\Lambda=0.25$ while remaining relatively flat, particularly for $\Lambda=1$. When the cavity is operated at belt speeds beyond the limits shown in Fig. 9, the spectral content of the secondary flow can no longer be simply characterized by a single dominant frequency as the mixing flow regime develops.

In Fig. 10, the primary dimensionless spatial wave numbers (αL), measured via LDV and photographic analyses are plotted against the Deborah number and the Weissenberg number respectively (based on the steady shear relaxation time). The spatial wave number α is extracted from Fourier analysis of the rapid LDV scans of $v_y(z)$ and $v_x(z)$ in the neutral z-direction of the cell and they monotonically increase with increasing De_s and Wi_s, consistent with our flow visualization observations. The wave numbers are consistently higher in smaller aspect ratios and, as observed in Fig. 5, the spatial frequency for deep cavities with higher aspect ratios $\Lambda=2,3$ remain similar to the $\Lambda=1$ case. Increasing the Deborah number beyond the limits shown in Fig. 10 creates a mixing flow in which many spatial modes are excited, making accurate determination of the primary spatial wave number difficult.

IV. OPERATING STABILITY DIAGRAMS

Cavity flows are encountered in many important industrial processes and the knowledge of the boundaries of its operating stability for a given fluid formulation has important design and processing implications.[2] In Fig. 11, the critical Deborah number is plotted versus the aspect ratio for both PIB fluids. For completeness, the Deborah numbers defined with both time constants λ_s and λ_r are shown on the left and right ordinate axes, respectively. Within the accuracy of the experimental measurements, the data for both fluids show an excellent superposition. The critical Deborah numbers remain almost the same for aspect ratios greater than $\Lambda=1$, and decrease progressively for shallower cavities with small aspect ratios.

Recognizing the importance of both length scales L and H in the cavity geometry, an operating stability diagram can be developed by plotting the critical Weissenberg number against the critical Deborah number for all aspect ratios as shown in Fig. 12. For each aspect ratio, the operating line begins at the origin where the imposed velocity is zero ($U=0$) and the fluid is at rest. Increasing the imposed driving velocity U describes a unique set of operating conditions lying along a straight line which passes through the origin with a slope of Λ^{-1}. The stability boundary defines the regions of stable versus unstable operation of the lid-driven cavity for the range of aspect ratios $0.25 \leqslant \Lambda \leqslant 4.0$ considered in the present study. More data are clearly required for shallower cavity flows with smaller aspect ratios $\Lambda < 0.25$ to expand the process stability diagram. However, the present stability diagram in Fig. 12 spans most industrially important cases in coating and extrusion processes.

V. KINEMATIC CHARACTERISTICS OF THE UNSTABLE FLOW

The flow visualization photographs provide qualitative information on the global structure of the three-dimensional flow that develops in the neutral direction following onset of the elastic instability. However, further details of the transi-

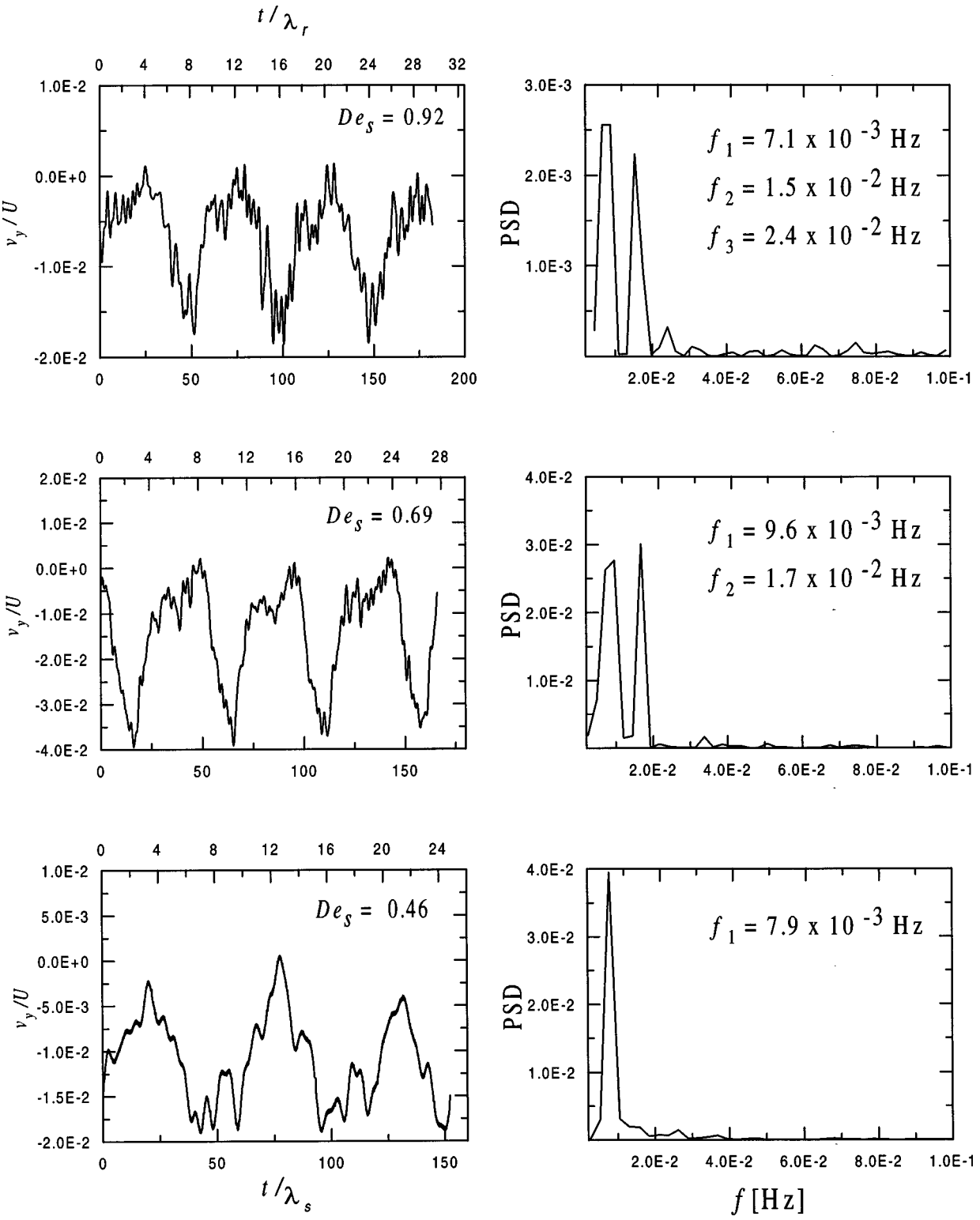

FIG. 8. Power spectral density (PSD) for the time-series measurements of the y-component of the fluid velocity at $x/L=0.5$, $y/H=0.8$, $z=0.0$ in a square cavity ($\Lambda=1$).

tion from the stable to unstable region and of the symmetries and kinematic characteristics of the resulting unsteady flow are needed to make a more clear assessment of the mechanisms that drive the growth of the observed temporal and spatial disturbances.

In Fig. 13, streak images of the flow field in the x-y plane following onset of the cellular instability are shown for aspect ratios of $\Lambda=0.5$, 1 and 2. The exposure times of these images are less than 1 second and are very small compared to the period of the traveling wave disturbances propagating in the neutral z-direction (orthogonal to the imaging plane). Hence the streaklines in these images appear smooth and two

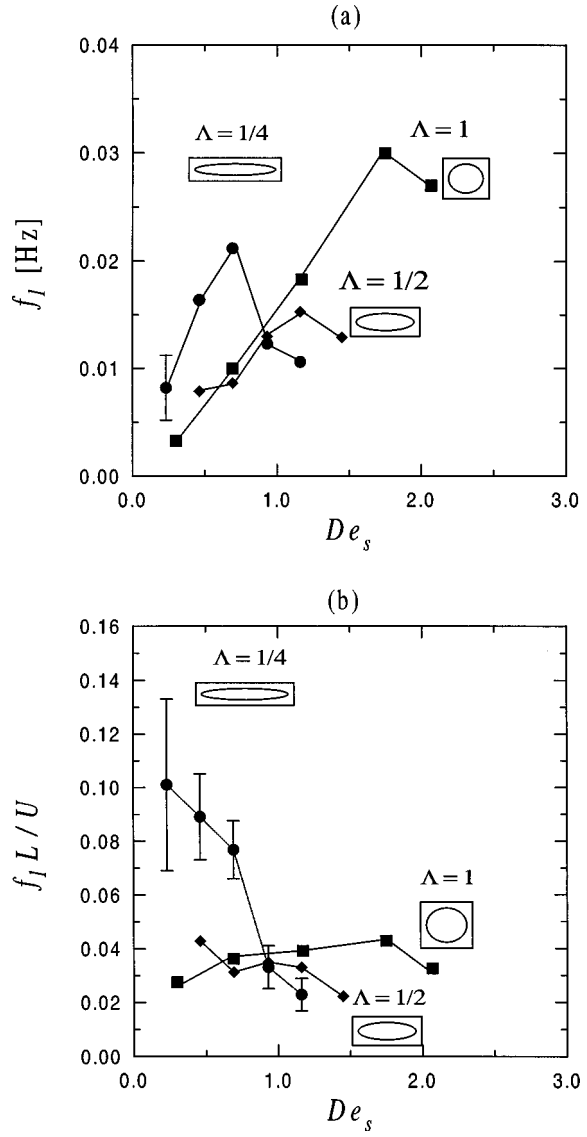

FIG. 9. (a) Dimensional and (b) dimensionless temporal frequency of the primary mode of elastic instability in cavity flows with aspect ratios $\Lambda = 0.25$, $\Lambda = 0.5$, and $\Lambda = 1.0$ as a function of Deborah number for 0.35 wt. % PIB solution. The error bars indicate the spectral resolution limit of the FFT analysis.

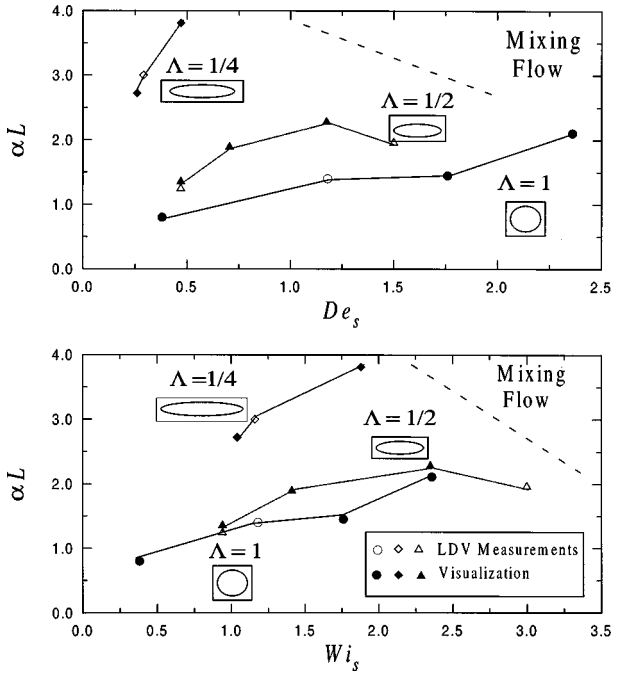

FIG. 10. Dimensionless spatial wave numbers of secondary flow in cavity flows with aspect ratios $\Lambda = 0.25$, 0.5, and 1.0 as a function of Deborah and Weissenberg numbers. The data include LDV measurements (hollow symbols) and photographic image analysis (solid symbols) for 0.35 wt. % PIB solution.

dimensional. In all cases the fore-aft symmetry about the line $x = 0.5L$, observed for the creeping motion of Newtonian liquids in the corresponding cavity geometry, is broken. The upstream shift of the geometric center of the main core vortex flow is enhanced compared to that reported previously in steady two-dimensional flows at lower Deborah numbers.[15] Laser Doppler measurements of the out-of-plane component of the velocity field at the critical conditions indicate that the instability is initiated in the vicinity of the downstream corner where the curvature of the fluid streamlines is most enhanced.

This region is highlighted by the black box in the streak photographs. The similarity in each image is readily apparent and, furthermore, it is clear that the representative radius of curvature of the streamlines in this region is not solely characterized by either the height H or width L of the test cell.

In Fig. 14 an approximate DPIV analysis of the velocity field in the y-z plane at $x/L = 0.5$ is attempted. The direction of the imposed velocity U is outward from the illuminated plane; however the out-of-plane displacement occurring in the time interval of 1/30th s is smaller than the thickness of the laser light sheet, hence we are able to resolve the in-plane components of the three-dimensional trajectories of the seed particles in each subimage. In the stable flow regime, the dominant component of the vectorial fluid velocity at the midplane $x/L = 0.5$ is projected in the x-direction and therefore DPIV observations in the y-z plane generate null displacement cross-correlations indicating no in-plane motion. Following the onset of instability, the y- and z-components

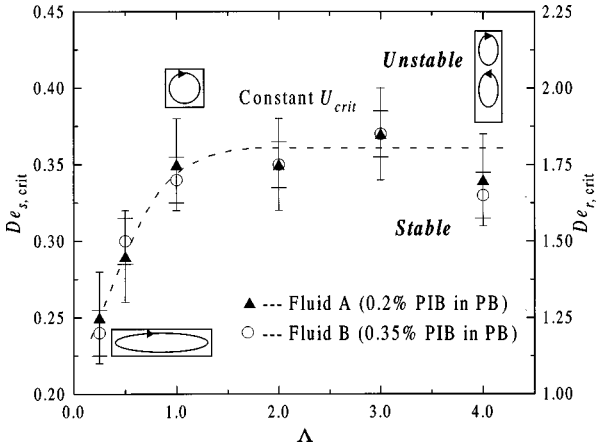

FIG. 11. The critical Deborah number $De_{s,crit}$ and $De_{r,crit}$ (based on the relaxation times λ_s and λ_r, respectively) as a function of aspect ratio Λ for both PIB fluids.

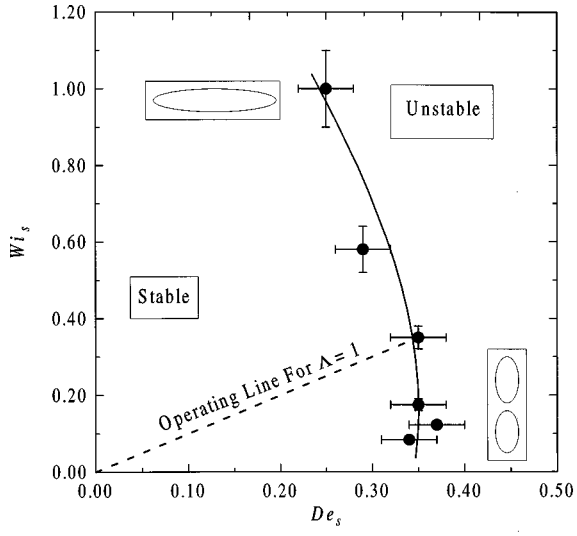

FIG. 12. An operating stability diagram for isothermal viscoelastic cavity flows. The solid line divides the stable and unstable operating regions.

of the secondary flow are apparent in the DPIV measurements as shown in Fig. 14. This measurement is, of course, only an instantaneous snap shot of the evolving spatial structure in the cavity geometry but it shows the complexity of the traveling waves in the flow domain. A similar technique has been used very recently by Baumert *et al.*[34] to resolve secondary cellular structures in the viscoelastic Taylor–Couette instability.

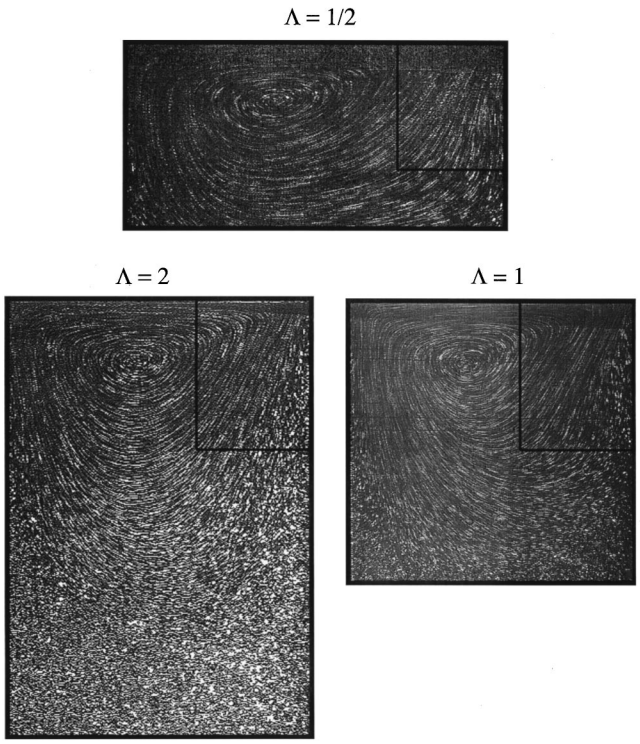

FIG. 13. Streak images of the fluid streamlines for cavity flows of the PIB solution with aspect ratios of $\Lambda=0.5$, $\Lambda=1.0$, and $\Lambda=2.0$. The Deborah number is $De_s=1.2$ for all cases. The highlighted areas are the downstream corner regions where the instability initiates.

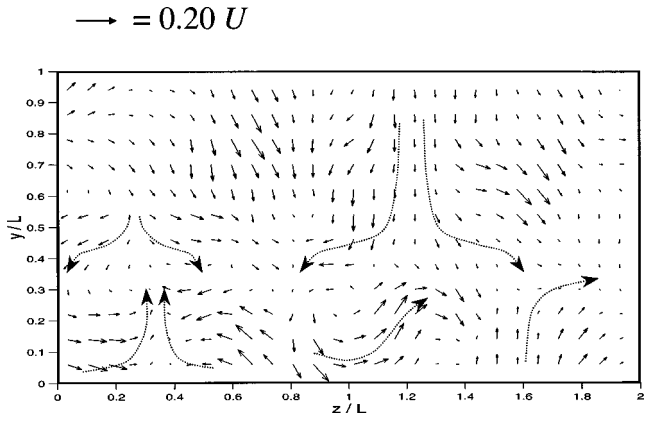

FIG. 14. DPIV measurements of the time-dependent secondary flow on the plane $x/L=0.5$ that develops following onset of elastic instabilities in a square cavity at $De_s=1.5$. The imposed velocity is normal to the plane of view and in the outward direction. The dashed lines are used to illustrate the fluid trajectories and are not DPIV measurements.

VI. DISCUSSION

We have documented the onset of purely elastic instabilities in cavity flows of Boger fluids in moderate aspect ratios ($0.25\leqslant\Lambda\leqslant4.0$). Complementary experimental observations have also been reported by Grillet and Shaqfeh[31] in recirculating flows of ideal elastic Boger fluids in the semi-cavity problem ($\Lambda\to0$). The structural patterns of these instabilities are similar to the purely elastic instabilities observed in the Taylor–Couette device, planar contraction flows, and the stagnation flow in the wake of a stationary cylinder. These instabilities are characterized by evolution of a three-dimensional motion in the neutral direction which, through flow visualization, appear as cellular structures similar to those presented in Figs. 3, 4, and 5.

As our LDV time-series measurements indicate (Fig. 7), the elastic instability is time dependent, initially having very long periods on the order of several hundreds of seconds. By contrast, Grillet and Shaqfeh[31] report that for the semi-cavity flow, the secondary flow that develops at small supercritical Deborah numbers appears to be stationary. However, it is important to note that the aspect ratios W/H in the neutral direction for these two sets of experiments are substantially different. Recent experimental observations in the planar contraction geometry have also shown that the mode of instability (i.e., traveling or standing waves) is modified by the aspect ratio of the flow cell in the neutral direction.[38] Previous linear stability analyses in the Taylor–Couette geometry[30] have shown that for a Couette cell of infinite axial length both traveling and standing waves are admissible modes of elastic instability for an Oldroyd-B fluid, and recent numerical studies on the effects of eccentricity in this geometry have shown that even very small geometric imperfections can have a pronounced effect on the most unstable mode of the resulting elastic instability.[39] Since the period of our measured velocity fluctuations close to the onset conditions is much longer than any fluid relaxation time scale our experimental observations suggest that for a two-dimensional cavity with $W/H\to\infty$, where the effect of end walls are entirely absent, the elastic instability may initially

develop in the form of standing waves. Clearly, further experimental investigations in cavities with fixed aspect ratio, $\Lambda = L/H$, but with varying aspect ratio *in the neutral direction*, W/H, are required to resolve this question.

Within the resolution of our experimental apparatus, no detectable hysteresis effect was observed and all instabilities were supercritical. The hysteresis is, of course, a complex phenomenon and it could occur within a very small window of operating conditions which is experimentally difficult to conclusively detect. Certainly numerical stability analysis is needed to clarify the behavior of the three-dimensional time-dependent solution of the equations of motion, near, or at, the critical onset conditions.

The spatial frequencies of the secondary flow that develops at the onset conditions appear to be independent of the neutral direction aspect ratio W/H as observed in Figs. 3 and 4. The spatial frequencies are, however, strongly affected by the variation in the aspect ratio Λ. From Figs. 3 to 6, it can be seen that the number of distinct cellular structures observed for $\Lambda = 3,2,1,0.5,0.25$ are 2, 2, 2, 4–5, 11–12, respectively. The functional dependency of the spatial wave number on Λ is complex because the aspect ratio is a relevant dynamic parameter only when both length scales H and L equally affect the local configuration of the planar two-dimensional base flow. In the limiting cases of deep slots ($\Lambda \ll 1$) or shallow cavities ($\Lambda \geqslant 1$) only one length scale affects the fluid kinematics, and therefore any scaling argument should be able to explain these limiting cases.

In general, the spatial frequencies increase with increasing Deborah and Weissenberg numbers as shown in Fig. 10. Upon transition to the mixing regime ($\mathrm{De} \geqslant 3\mathrm{De}_{\mathrm{crit}}$), it is experimentally difficult to decompose the spatial frequency into a single predominant mode, since many higher frequency disturbances are also excited and mask the primary mode. The kinematical structure of these instabilities is similar to the Taylor–Görtler vortices observed following onset of inertially driven hydrodynamic instabilities in Newtonian cavity flows.[2] The DPIV snapshot of the flow field, presented in Fig. 14, is also consistent with the laser light-sheet flow visualization of Grillet and Shaqfeh.[31] Both observations indicate the existence of a ''mushroomlike'' structure which possibly arises from the pairwise interactions of weak traveling vortices near the floor of the cavity. Nonlinear stability calculations have shown that similar structures evolve to form Görtler vortices in Newtonian fluids and these structures lead to the rapid mixing of fluid regions with high and low momentum.[4]

As we have argued previously,[15] the kinematics of the two-dimensional flow in the downstream corner play an important role in characterizing the critical onset conditions. The two-dimensional view of the unstable flow shown in Fig. 13 illustrates the key corner region where these elastic instabilities initiate. At the critical onset conditions it is clear that the spatial structure of the primary flow in this region is very similar regardless of the global aspect ratio of the cavity. At high Deborah numbers, the fore-aft asymmetry of the base two-dimensional flow becomes increasingly apparent: The center of the core vortex flow shifts in the upstream direction and the streamline radius of curvature in the downstream corner concomitantly decreases which, in turn, amplifies the magnitude of the streamwise hoop stress ($\tau_{\theta\theta}$), and its gradient ($\tau_{\theta\theta}/r$) in this region. Here, r is a local coordinate normal to the fluid streamline that characterizes the radius of curvature of the streamline and $\tau_{\theta\theta}$ is the $\theta\theta$-component of polymeric stress. In curvilinear coordinates terms such as $\tau_{\theta\theta}$ and $\tau_{\theta\theta}/r$ provide the coupling mechanism between the individual components of the momentum equation and the convected derivatives of stress appearing in quasilinear constitutive equations. In their study of the purely elastic instability arising in Taylor–Couette flow, Larson *et al.*[17] point out that the systematic increase in the magnitude of such terms with increasing shear rate is the primary physical mechanism for driving the elastic instability. Similar couplings between the kinematics and radial gradients in the hoop stresses lead to instabilities in Taylor–Dean flows of elastic fluids.[40]

In more complex two-dimensional flows such as the cavity flow considered here, both the curvature of the fluid streamlines and the magnitude of the polymeric hoop stress vary throughout the flow domain. Recently, a dimensionless criterion for unifying the critical onset conditions of elastic instabilities in various flow geometries has been proposed.[32] This criterion for onset of elastic instability can be written in the following form,

$$\left\{ \frac{l}{\mathscr{R}} \mathrm{Wi}_s \right\} \geqslant M^2_{\mathrm{crit}}, \tag{6.1}$$

where $l \equiv \lambda_s U$ is interpreted as the characteristic length scale over which the perturbations to the viscoelastic base flow relax, and $\mathscr{R}$ as the characteristic streamline radius of curvature in the system. At the critical conditions, this dimensionless group attains a critical magnitude M^2_{crit}, beyond which the flow is unstable.

In many unidirectional flow geometries, such as flows generated in a cone-plate rheometer, between two concentric parallel disks, and in the Taylor–Couette geometry, the characteristic streamline radius of curvature can be readily identified. More importantly, the streamline radius of curvature remains constant when the magnitude of the imposed driving velocity is increased. However, in more complex flows such as the cavity flow, the streamline radius of curvature varies throughout the flow geometry and is furthermore a function of the imposed velocity or throughput. Under such circumstances, a simple scaling expression can be constructed to quantify the streamline radius of curvature by combining the principal radii of curvature of any two-dimensional flow field in the form

$$\frac{1}{\mathscr{R}} = \frac{a}{L} + \frac{b}{H}, \tag{6.2}$$

where a and b are two dimensionless weighting parameters that identify the relative importance of the two primary length scales L and H in modulating the geometrical structure of the flow.

A more detailed study[33] provides further insight into this dimensionless criterion and applies the formula successfully

to a broad selection of experimental and theoretical case studies. In this work the proposed dimensionless group is expressed in a more general form as

$$\left(\frac{\lambda_s U}{\mathscr{R}}\frac{\tau_{11}}{\tau_{12}}\right) \geqslant M^2_{\text{crit}}, \tag{6.3}$$

where τ_{11} is the tensile stress in the local streamwise direction, and $\tau_{12} \sim \eta_0 \dot{\gamma}$ is the characteristic shear stress across the stream lines. This definition, which provides an explicit definition for the Weissenberg number in terms of a stress ratio, can be obtained directly from dimensional consideration of the convected derivative terms encountered in quasilinear and nonlinear constitutive equations. The dimensionless criterion in Eq. (6.3) can also be extended to include a spectrum of relaxation times and, more importantly, the effect of shear thinning in the material properties.[33]

If we follow a fluid element along a closed streamline, then the streamwise tension τ_{11} will decrease, and can even change sign, as fluid particles pass through regions of local (Lagrangian) deceleration. In these regions, Eq. (6.3) suggests that the flow is stable in agreement with our experimental observation. By contrast, regions characterized by curved streamlines coupled with strong streamwise acceleration are expected to be prone to elastic instability. The spatial variation of the scalar magnitude of M^2 in a stagnation flow has recently been investigated by Öztekin *et al.*[41]

In the cavity geometry, the instability initiates in the downstream corner where the streamlines of the base flow exhibit significant curvature, and fluid elements accelerate away from the corner. In this region, the deformation rate scales with $\dot{\gamma} = U/\mathscr{R}$, which defines a local Weissenberg number $Wi_{s,\mathscr{R}} = \lambda_s U/\mathscr{R}$. Substituting the local Weissenberg number and Eq. (6.2) into Eq. (6.1), we arrive at the following equation at the critical onset conditions,

$$\lambda_s U_{\text{crit}}\left(\frac{a}{L}+\frac{b}{H}\right) = M_{\text{crit}}. \tag{6.4}$$

Rearranging terms, we obtain

$$\tilde{a}\Lambda + \tilde{b} = \frac{1}{\text{Wi}_{s,\text{crit}}}, \tag{6.5}$$

with $\tilde{a} = a/M_{\text{crit}}$ and $\tilde{b} = b/M_{\text{crit}}$. Although $\tilde{a}$ and $\tilde{b}$ are unknown *a priori*, the reciprocal of the critical Weissenberg number at the onset of instability is thus expected to be a linear function of the aspect ratio Λ.

In Fig. 15, the critical Weissenberg number is plotted against the aspect ratio and there is an excellent agreement with the proposed dimensionless scaling analysis.[32,33] The experimental measurement of Grillet and Shaqfeh[31] for a semi-infinite cavity geometry ($\Lambda \to 0$) can also be represented in this form, and is shown in Fig. 15 by the asterix close to the abscissa. Clearly this experimental observation, which was performed with a very similar Boger fluid, is also consistent with the proposed form of the stability criterion. Since Eq. (6.4) involves three dimensionless parameters and only two values may be determined from linear regression of the experimental data in Fig. 15, it is not possible to unambiguously determine the critical magnitude of the proposed

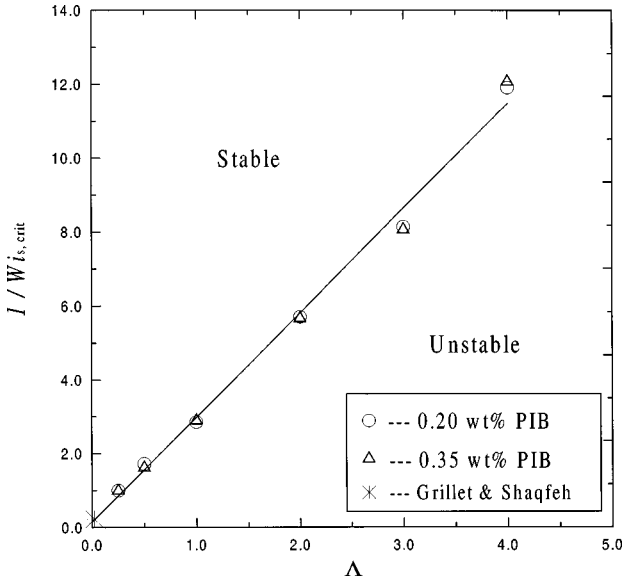

FIG. 15. Reciprocal of the critical Weissenberg number as a function of the cavity aspect ratio showing a linear relationship as predicted by the dimensionless stability criterion. The data point marked by (*) is from the measurements of Grillet and Shaqfeh (Ref. 31).

stability criterion, M_{crit}, without consideration of a numerical linear stability analysis. As $\Lambda \to 0$ the critical onset condition reduces to $\tilde{b} = 0.14$ or $\text{Wi}_{s,\text{crit}} = 7.2$.

As we have documented in the present study, there is a rich dynamical structure in the cavity flow of non-Newtonian fluids. The scaling arguments proposed recently[32,33,42] can be used to systematically describe the effects of fluid rheology and geometry on the operational stability of isothermal lid-driven cavity flows. Ultimately the critical conditions represented by a criterion such as Eq. (6.3) may even be utilized in a predictive or design capacity to expand the operational capabilities of processing operations involving complex flows of viscoelastic liquids. Screw extruders embody many of the kinematic elements of cavity flows, however such processes are commonly nonisothermal, and it would be of interest to extend these arguments to such processes.

ACKNOWLEDGMENTS

This research was supported by National Science Foundation Grant No. CTS9553216 to G. H. McKinley. The authors would like to thank Dr. Stephen Spiegelberg for assistance in constructing the flow cell and the anonymous reviewers for their insightful comments.

[1] N. Ramanan and G. M. Homsy, ''Linear stability of lid-driven cavity flow,'' Phys. Fluids **6**, 2690 (1994).
[2] C. K. Aidun, ''Principles of hydrodynamic instability: Application in coating systems, Part 2: Examples of flow instability,'' Tappi J. **74**, 213 (1991).
[3] G. I. Taylor, ''Stability of a viscous liquid contained between rotating cylinders,'' Philos. Trans. R. Soc. London, Ser. A **223**, 289 (1923).
[4] S. W. Saric, ''Görtler instabilities,'' Annu. Rev. Fluid Mech. **26**, 379 (1994).
[5] C. K. Aidun, A. Triantafillopoulos, and J. D. Benson, ''Global stability of lid-driven cavity with throughflow: Flow visualization studies,'' Phys. Fluids A **3**, 2081 (1991).
[6] C. W. Leong and J. M. Ottino, ''Increase in regularity by polymer addition

during chaotic mixing in two-dimensional flows,'' Phys. Rev. Lett. **64**, 874 (1990).
[7]D. V. Boger, ''A highly elastic constant-viscosity fluid,'' J. Non-Newtonian Fluid Mech. **3**, 87 (1977/78).
[8]T. C. Niederkorn and J. M. Ottino, ''Mixing of a viscoelastic fluid in a time-periodic flow,'' J. Fluid Mech. **256**, 243 (1993).
[9]S. Kurnar and G. M. Homsy, ''Chaotic advection in creeping flow of viscoelastic fluids between slowly modulated eccentric cylinders,'' Phys. Fluids **8**, 1774 (1996).
[10]M. P. Reddy and J. N. Reddy, ''Finite-element analysis of flows of non-Newtonian fluids in three-dimensional enclosures,'' Int. J. Non-Linear Mech. **27**, 9 (1992).
[11]P. Isaksson and M. Righdal, ''Numerical simulation of blade coating with short dwell and roll application coaters,'' Rheol. Acta **33**, 454 (1994).
[12]M. A. Mendelson, P.-W. Yeh, R. A. Brown, and R. C. Armstrong, ''Approximation error in finite element calculation of viscoelastic fluid flows,'' J. Non-Newtonian Fluid Mech. **10**, 31 (1982).
[13]R. B. Bird, R. C. Armstrong, and O. Hassager, *Dynamics of Polymeric Liquids, Vol. 1* (Wiley, New York, 1987).
[14]R. R. Huilgol, ''On uniqueness and nonuniqueness in the planar creeping flows of second order fluids,'' SIAM (Soc. Ind. Appl. Math.) J. Appl. Math. **24**, 226 (1973).
[15]P. Pakdel, S. H. Spiegelberg, and G. H. McKinley, ''Cavity flows of viscoelastic fluids: Two-dimensional flows,'' Phys. Fluids **9**, 3123 (1997).
[16]H. Giesekus, ''Zur Stabilitat von Stromungen viscoelastischen Flussigkeiten,'' Rheol. Acta **5**, 239 (1966).
[17]S. J. Muller, R. G. Larson, and E. S. J. Shaqfeh, ''A purely elastic transition in Taylor–Couette flow,'' Rheol. Acta **28**, 449 (1989).
[18]R. G. Larson, S. J. Muller, and E. S. J. Shaqfeh, ''A purely elastic instability in Taylor–Couette flow,'' J. Fluid Mech. **218**, 573 (1990).
[19]E. S. J. Shaqfeh, S. J. Muller, and R. G. Larson, ''The effects of gap width and dilute solutions properties on the viscoelastic instability,'' J. Fluid Mech. **235**, 325 (1992).
[20]R. Sureshkumar, A. N. Beris, and M. Avgousti, ''Non-axisymmetric subcritical bifurcations in viscoelastic Taylor–Couette flow,'' Proc. R. Soc. London, Ser. A **447**, 135 (1994).
[21]N. Phan-Thien, ''Cone and plate flow of the Oldroyd-B fluid is unstable,'' J. Non-Newtonian Fluid Mech. **17**, 37 (1985).
[22]G. H. McKinley, J. A. Byars, R. A. Brown, and R. C. Armstrong, ''Observations on the elastic instability in cone-and-plate and parallel-plate flows of polyisobutylene Boger fluid,'' J. Non-Newtonian Fluid Mech. **40**, 201 (1991).
[23]G. H. McKinley, A. Öztekin, J. A. Byars, and R. A. Brown, ''Self-similar spiral instabilities in the elastic flows between a cone and a plate,'' J. Fluid Mech. **285**, 123 (1995).
[24]D. A. Olagunju, ''Elastic instabilities in cone and plate flow: Small gap theory,'' Z. Angew. Math. Phys. **46**, 946 (1995).
[25]A. Öztekin, G. H. McKinley, and R. A. Brown, ''Quantitative prediction of the viscoelastic instability in cone-and-plate flow of a Boger fluid using a multi-mode Giesekus model,'' J. Non-Newtonian Fluid Mech. **54**, 351 (1994).
[26]A. Avagliano and N. Phan-Thien, ''Torsional flow: Elastic instability in a finite domain,'' J. Fluid Mech. **312**, 279 (1996).
[27]G. H. McKinley, W. P. Raiford, R. A. Brown, and R. C. Armstrong, ''Non-linear dynamics of viscoelastic flow in axisymmetric abrupt contractions,'' J. Fluid Mech. **223**, 411 (1991).
[28]G. H. McKinley, R. C. Armstrong, and R. A. Brown, ''The wake instability in viscoelastic flow past confined circular cylinders,'' Philos. Trans. R. Soc. London, Ser. A **344**, 265 (1993).
[29]R. G. Larson, ''Instabilities in viscoelastic flows,'' Rheol. Acta **31**, 213 (1992).
[30]E. S. G. Shaqfeh, ''Purely elastic instabilities in viscometric flows,'' Annu. Rev. Fluid Mech. **28**, 129 (1996).
[31]A. M. Grillet and E. S. G. Shaqfeh, ''Observations of viscoelastic instabilities in recirculation flows of Boger fluids,'' J. Non-Newtonian Fluid Mech. **64**, 141 (1996).
[32]P. Pakdel and G. H. McKinley, ''Elastic instability and curved streamlines,'' Phys. Rev. Lett. **77**, 2459 (1996).
[33]G. H. McKinley, P. Pakdel, and A. Öztekin, ''Geometric and rheological scaling of purely elastic flow instabilities,'' J. Non-Newtonian Fluid Mech. **67**, 19 (1996).
[34]B. M. Baumert and S. J. Muller, ''Flow regimes in model viscoelastic fluids in a circular Couette system with independently rotating cylinders,'' Phys. Fluids **9**, 566 (1997).
[35]P. Pakdel and G. H. McKinley, ''Digital Particle Image Velocimetry of Viscoelastic Fluids,'' AIChE. J. **43**, 289 (1997).
[36]L. M. Quinzani, G. H. McKinley, R. A. Brown, and R. C. Armstrong, ''Modeling the rheology of polyisobutylene solutions,'' J. Rheol. **34**, 705 (1990).
[37]R. G. Larson, S. J. Muller, and E. S. G. Shaqfeh, ''The effect of fluid rheology on the elastic Taylor–Couette instability,'' J. Non-Newtonian Fluid Mech. **51**, 195 (1994).
[38]L. Genieser, ''Viscoelastic instabilities in abrupt contraction flows,'' Ph.D. Thesis, Department of Chemical Engineering, Mass. Inst. of Tech., 1997.
[39]A. Chawda and M. Avgousti, ''Stability of viscoelastic flow between eccentric rotating cylinders,'' J. Non-Newtonian Fluid Mech. **63**, 97 (1996).
[40]Y. L. Joo and E. S. G. Shaqfeh, ''Observations of purely elastic instabilities in the Taylor–Dean flow of a Boger fluid,'' J. Fluid Mech. **262**, 27 (1994).
[41]A. Öztekin, B. Alakus, and G. H. McKinley, ''Stability of planar stagnation flow of a highly viscoelastic fluid,'' J. Non-Newtonian Fluid Mech. **72**, 1 (1997).
[42]G. H. McKinley, ''Extensional Flow and Instabilities of Elastic Polymer Solutions,'' to appear in *Dynamics of Complex Fluids; Proceedings of the Royal Society/Unilever Indo-UK Forum*, edited by M. J. Adams (ICL Press, London, 1998).